Pal, Pinki; Kaur, Amadeep; Suihkonen, Sami; Lemettinen, Jori; Laha, A.; Dhar, Subhabrata; Mahapatra, Suddhasatta

Enhanced Specific Detectivity and UV-to-Visible Rejection-Ratio of Visible-Blind Metal–Semiconductor–Metal Photodetectors, Based on Epitaxial GaN/Si(111)

Published in:
IEEE Transactions on Electron Devices

DOI:
10.1109/TED.2023.3277798

Published: 05/06/2023

Document Version
Peer-reviewed accepted author manuscript, also known as Final accepted manuscript or Post-print

Enhanced Specific Detectivity and UV-to-Visible Rejection-Ratio of Visible-Blind Metal–Semiconductor–Metal Photodetectors, Based on Epitaxial GaN/Si(111)

Pinki Pal, Amandeep Kaur, Sami Suihkonen, Jori Lemettinen, Apurba Laha, Subhabrata Dhar, and Suddhasatta Mahapatra

***Abstract*— A very high specific detectivity and UV-to-visible rejection-ratio (UVRR) is reported for visible-blind metal–semiconductor–metal (MSM) photodetectors (PDs), fabricated with gallium nitride (GaN) on Si(111) epitaxial layers. Comprehensive analysis of different figures-of-merit (FOM) reveals that the high specific detectivity results from a large responsivity in the UV-A region of the electromagnetic spectrum, and extremely low dark current, of the PDs. The current transport mechanisms in the absence and presence of illumination suggest that an internal gain, which is attributable to photo-induced barrier lowering, is responsible for the large responsivity of the PDs. The dark current is reduced due to the use of platinum-gold (Pt/Au) Schottky contacts, characterized by a relatively high Schottky barrier height. The vast improvement of nearly all FOMs, compared to those reported earlier for GaN/Si PDs, is highly encouraging for the development of low-cost, large-area arrays of visible-blind PDs.**

***Index Terms*— Direct tunneling, epitaxy, gallium nitride (GaN), Poole–Frenkel (PF) effect, responsivity, specific detectivity, thermionic emission (TE), thermionic field emission, UV-to-visible rejection-ratio (UVRR), visible-blind photodetectors (PDs).**

I. INTRODUCTION

THE III-nitride family of semiconductors, and their alloys, have emerged as an attractive material system for the development of optoelectronic devices, for wavelengths spanning from the infrared to the deep ultraviolet region of the electromagnetic spectrum [1], [2], [3], [4], [5]. In particular, gallium nitride (GaN) is highly promising for the development of visible-blind ultra-violet (UV) photodetectors (PDs), owing to its wide (direct) band gap of 3.4 eV, and robust chemical and thermal stability. Such UV-PDs are much-coveted for commercial, space, and military applications, such as UV astronomy, space-communication, flame detection, ozone layer monitoring, and sensing in harsh working environments [6], [7], [8]. Over the past couple of decades, a large variety of GaN-based PDs have been proposed and developed, including (p-n and p-i-n) junction photodiodes [9], [10], [11], [12], Avalanche photodiodes [13], Schottky-barrier photodiodes [14], [15] and metal–semiconductor–metal (MSM) PDs [16], [17], [18], [19], [20], [21], [22], [23], [24], [25], [26], [27], [28], [29], [30], [31], [32]. However, further work is needed to optimize the crucial performance metrics of GaN-based PDs, especially for those fabricated with economical GaN epitaxial layers grown on silicon (Si) substrates. Due to the large lattice- and thermal-conductivity mismatch between GaN and Si, obtaining high-quality large-area GaN/Si(111) epitaxial layers is non-trivial. Nevertheless, recent advances in controlling the threading dislocation density (TDD) of GaN/Si(111) epilayers have fueled considerable interest in the fabrication of robust and cost-effective visible-blind UV PDs.

In this work, we report the fabrication and characterization of GaN/Si(111) inter-digitated MSM PDs, demonstrating a record-high specific detectivity of 4.93×10^{14} Jones, at 355 nm. The high specific detectivity results from the extremely low dark current ($\sim$ few to few 100 pA, at bias voltages of up to ± 40 V) and high responsivity (>250 A/W at 353 nm) of the fabricated MSM PDs, with platinum–gold (Pt/Au) Schottky contacts. The maximum UV-to-visible rejection-ratio (UVRR) is $>10^5$, while the rise time of PDs is ~ 55 μs. The report also provides valuable insight into the carrier transport mechanisms operating at different regimes of bias voltages, both in the presence and absence of UV illumination.

Manuscript received 12 January 2023; revised 22 March 2023; accepted 11 May 2023. This work was supported by the Ministry of Electronics and Information Technology (MeitY), Government of India (GoI). The review of this article was arranged by Editor S.-C. Shen. *(Corresponding author: Suddhasatta Mahapatra.)*

Pinki Pal, Amandeep Kaur, Subhabrata Dhar, and Suddhasatta Mahapatra are with the Department of Physics, IIT Bombay, Mumbai 400076, India (e-mail: palpinki0454@gmail.com; deepamankaur57.ak@gmail.com; dhar@phy.iitb.ac.in; suddho@phy.iitb.ac.in).

Sami Suihkonen and Jori Lemettinen are with the Department of Electronics and Nanoengineering, Aalto University, 00076 Aalto, Finland (e-mail: sami.suihkonen@aalto.fi; jori.lemettinen@gmail.com).

Apurba Laha is with the Department of Electrical Engineering, IIT Bombay, Mumbai 400076, India (e-mail: laha@ee.iitb.ac.in).

Color versions of one or more figures in this article are available at https://doi.org/10.1109/TED.2023.3277798.

Digital Object Identifier 10.1109/TED.2023.3277798

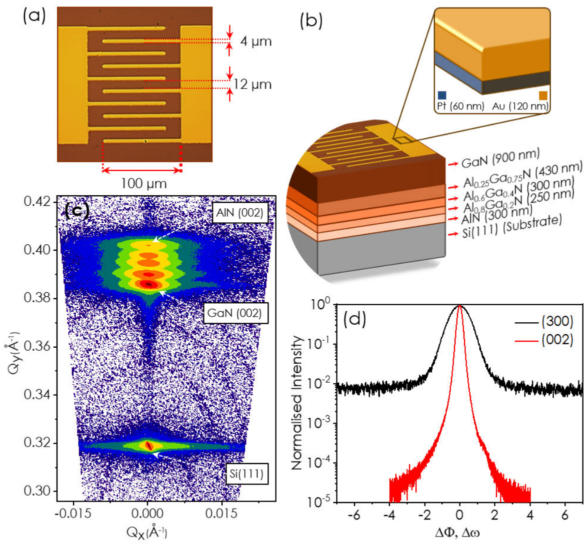

Fig. 1. (a) Optical microscope image of the MSM PD, showing the inter-digitated finger contacts, and part of the large contact pads. Dimensions of the finger-contacts, as well as their pitch, are depicted in this figure. (b) Schematic of the MOVPE-grown III-N stack on Si(111) substrate, terminated by a 900-nm-thick GaN layer. The compositions and thicknesses of the different AlGaN layers, as well as the initially-grown AlN layer, are mentioned. The inset shows, schematically, the Pt (60 nm)/Au (120 nm) metal stack, used to make the finger-contacts and the contact pads of the MSM PDs. (c) Reciprocal space map showing the intensity distributions corresponding to the Si(111) reflection and the different III-Nitride (002) reflections. (d) HRXRD rocking curves recorded for the out-of-plane (002) and the in-plane (300) diffraction peaks of GaN.

II. Experiments

The complete layout of the epitaxial III-Nitride heterostructure, with a 900-nm-thick, unintentionally-doped (UID) GaN layer on top, is schematically shown in Fig. 1(b). Details of the metal-organic vapor phase epitaxy (MOVPE) growth of the sample are published in [20]. To realize the MSM PDs, interdigitated contacts (IDCs) were fabricated by a combination of UV photolithography, oxygen-plasma ashing, oxide-etching in 5:1 buffered-HF, and metal-stack deposition by dc sputtering. An optical-microscopy image of the IDT contacts, together with (sections of) the large contact pads for wire bonding, is superposed with the schematic representation of the III-nitride heterostructure in Fig. 1(b). The IDC consists of 4-μm-wide and 100-μm-long fingers, with consecutive fingers separated by 12 μm [Fig. 1(a)] with an active photosensitive area of 14 000 μm^2. The metal-stack consists of a 60-nm Pt layer in contact with the GaN layer, followed by 120-nm of Au [schematically shown in the inset of Fig. 1(b)].

The crystal quality of the grown epi-layers was studied in detail, combining ω–2θ scans, ω-rocking curves, and reciprocal space maps, obtained using a Rigaku SmartLab high-resolution X-ray diffraction (HRXRD) system. The carrier concentration and Hall-mobility of the UID GaN layer were evaluated using Hall-measurements. The dc photo-response measurements were performed using a 150-W Xenon white-light source, a Spectra high-throughput $f/3.5$ monochromator (with holographic 1200 l/mm precision grating), and a Keithley 2450 source measure unit. A UV-enhanced Si photodiode was used to obtain the spectral power distribution of the Xenon lamp. The temporal response of the PDs was recorded using an optical chopper (operated at 787 Hz), a 325-nm Hg–Cd laser, and a digital oscilloscope (with a bandwidth and sampling rate of 3 GHz and 2.5 GS/s).

III. Results and Discussion

Fig. 1(c) shows the RSM recorded from the sample around the (111) reflection of Si. Diffracted intensity distributions due to the Si substrate, the AlN starting layer, and the GaN device layer are labeled in Fig. 1(c). Intensity distributions between those of AlN and GaN correspond to the step-graded AlGaN buffer, consisting of three layers of different thicknesses and progressively lower Al content [as depicted in Fig. 1(b)]. The Al-content of the different layers of the step-graded AlGaN buffer was determined from wide-angle ω-2θ scans (not shown), while their thicknesses were obtained from cross-sectional scanning electron microscopy [20]. Lattice and thermal-expansion mismatches between Si(111) and GaN are minimized by the introduction of the AlN and the step-graded AlGaN buffer layers, resulting in suppression of the TDD [33], [34], [35], [36]. To obtain a reliable quantitative estimate of the TDD, ω-rocking scans were recorded for the out-of-plane (002) and in-plane (300) reflections of GaN, as shown in Fig. 1(d). From the full-width at half-maximum (FWHM) values of these diffraction peaks ($\Delta\omega$), the edge (ρ_E) and screw (ρ_S) dislocation densities were calculated from the expressions $\rho_E = (\Delta\omega^{(300)})^2/(2\pi \ln 2)\mathbf{b}_E^2$ and $\rho_S = (\Delta\omega^{(002)})^2/(2\pi \ln 2)\boldsymbol{b}_S^2$. Here, $\boldsymbol{b}_E = (1/3)\langle 11\bar{2}0\rangle)$ and $\boldsymbol{b}_S = \langle 0001\rangle$ are the Burgers vectors for edge and screw-type dislocations, respectively. We obtained $\rho_E = 9.91 \times 10^{10}$ cm^{-2} and $\rho_S = 2.13 \times 10^9$ cm^{-2}. These values are comparable to those reported previously [33], [34], [35], [36]. We obtained the unintentional n-type doping concentration of the GaN layer 7×10^{16}cm^{-3} and the mobility 200 cm$^2 \cdot$ V$^{-1}S^{-1}$.

To analyze the performance metrics of the fabricated MSM PDs, we first recorded the dark current characteristics over a large bias-voltage range of $\pm$40 V, and for temperatures varying from 298 to 473 K [Fig. 2(a)]. At room temperature, the dark current (I_D) remains in the order of a few hundred pA, even for bias voltages as high as $V_B = 40$ V. We note that with Ni/Au Schottky contacts, MSM PDs fabricated on the same GaN epitaxial layer showed a factor of 100–1000 larger dark current over the probed range of V_B [20]. This is not surprising considering the higher work function of Pt (5.65 eV), compared to Ni (5.05 eV).

The temperature dependence of the dark current–voltage (I–V) characteristics (I–V–T characteristics) provides insight into the carrier transport mechanisms, in our MSM PDs. We consider the MSM structures to be back-to-back Schottky diodes, wherein the reverse-biased Schottky contact determines the current for both bias polarities. Accordingly, we identify four different transport regimes, within the range of temperatures and bias voltages, depicted in Fig. 2(a). Thermionic emission (TE) appears to be dominant in the range between $V_B = 2$–10 V. As shown in Fig. 2(b), for the I–V plots recorded at 323 and 473 K, a good fit of the TE equation, $I_D^{(\mathrm{TE})} = A \times J_S \exp(qV_B/\eta k_B T)(1 - \exp[-(qV_B/k_B T)])$ is obtained for this V_B-range.

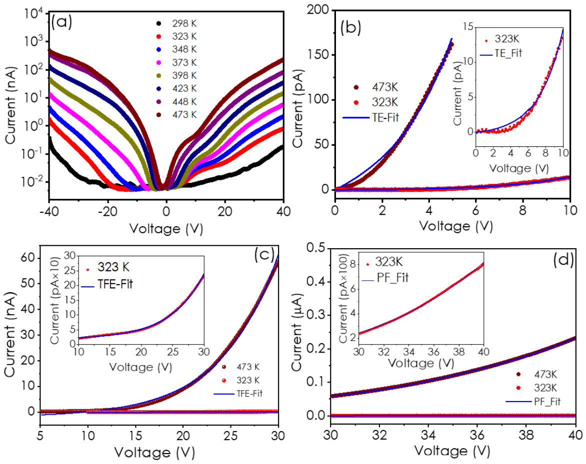

Fig. 2. (a) Temperature-dependent I–V–T characteristics of the MSM PDs. (b) Fitting of the TE transport equation, to the current measured over the bias range of $V_B = 0 - 10$ V, for $T = 323$ and 473 K. Inset: Close-up of the TE-fitting, for $T = 323$ K. (c) Fitting of the TFE transport equation, to the current measured over the bias range of $V_B = 5 - 30$ V, for $T = 323$ and 473 K. Inset: Close-up of the TFE-fitting for $T = 323$ K. (d) Fitting of the PF transport equation, to the current measured over the bias range of $V_B = 30 - 40$ V, for $T = 323$ and 473 K. Inset: Close-up of the PF-fitting for $T = 323$ K.

Here, $J_S = A^* \times T^2 \exp(\Phi_B/\eta kT)$ is the reverse saturation current density and $I_D^{(\mathrm{TE})}$ is the measured current, while T is the measurement temperature. A^*, Φ_B, n, and k_B are the Richardson constant, the zero-bias Schottky barrier height, the ideality factor, and Boltzmann's constant, respectively. Assuming $\eta = 1$, we obtained Φ_B to be equal to 994 meV, at 298 K. However, Φ_B increases to 1.3 eV at 473 K, indicating barrier height inhomogeneity at the metal–semiconductor interface, possibly due to interface roughness, point defects, and/or dislocations [37], [38], [39].

Below $V_B = 2$ V, the TE plot deviates from the measured values, even at 473 K. Due to the large Schottky barrier at the metal–semiconductor interface, the dark current in this bias range is possibly controlled predominantly by direct tunneling, even at elevated temperatures. On the other hand, the I–V characteristics recorded both at 323 and 473 K, over the bias range of 10–30 V, show a good fit to the thermionic field emission (TFE) model, wherein the dark current is expressed as $I_D^{(\mathrm{TFE})} = I_{00} \exp(qV_B/\varepsilon)$ [Fig. 2(c)]. Here, I_{00} is the saturation current, and $\varepsilon = [E_{00}/(E_{00}/k_B T) - \tanh(E_{00}/k_B T)]$, where E_{00} is a tunneling parameter that depends on the concentration and effective mass of the majority charge carrier and the dielectric constant of the semiconductor. From the fitting of the I–V plots, we obtain $E_{00} = 20.46$ and 41.06 meV, at 323 and 473 K, respectively. As both values are comparable to $k_B T$ at the respective temperatures, it may be concluded that TFE dominates the dark current in this bias range.

Finally, the relatively-weak dependence of I_D on V_B, in the range from 30 to 40 V, indicates the onset of the Poole–Frenkel (PF) effect. The PF effect is characterized by field-assisted carrier excitation from localized traps, into the continuum of conduction states. An excellent fit is obtained for the I–V plots recorded at both temperatures, with the PF equation, $I_D^{(\mathrm{PF})} = Aq\mu N_c E \exp(-q/k_B T[\Phi_T - (qE/\pi\varepsilon_0\varepsilon_S)^{1/2}])$, as shown in Fig. 2(d). Here, A is the device area, μ is the carrier drift-mobility, N_c is the density of states in the conduction band or the continuum, $q\Phi_T$ is the trap energy level, E is the electric field, ε_S is the high-frequency relative permittivity of the semiconductor, and ε_0 is the permittivity of vacuum. From the fitting, we obtain $\phi_T = 670$ meV and $\epsilon_s = 4.06$, at 473 K. The latter is in good agreement with reported values for GaN [40].

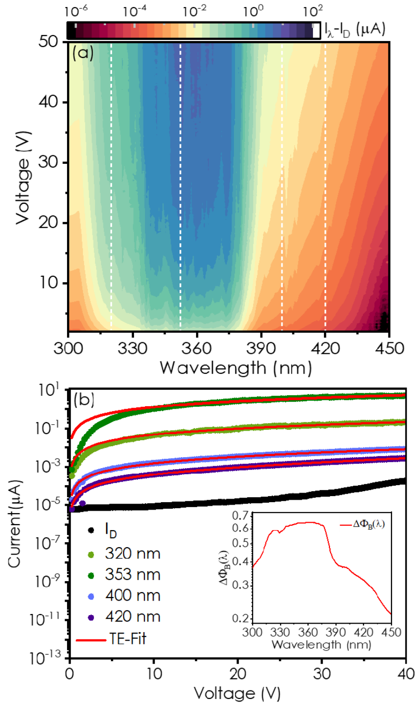

Fig. 3. (a) Colormap of the measured photocurrent [after subtracting the dark current (I_D)], as a function of the applied bias (V_B) and the wavelength (λ) of the incident radiation. (b) I–V characteristics under illumination at four different wavelengths [denoted by the white dashed lines in the colormap of (a)], together with the I_D measured over the entire range of V_B.

Next, we focus on the photoresponse of the fabricated MSM detectors. Fig. 3(a) shows a colormap of the obtained photocurrent, as a function of both V_B and the wavelength (λ) of the incident radiation. For all λ, the photocurrents have been plotted after subtracting the I_D-component, at each V_B. On the other hand, Fig. 3(b) shows the measured I–V characteristics, at four specific wavelengths, corresponding to the dotted lines in Fig. 3(a).

Also shown in Fig. 3(b) is the plot of I_D, measured over the same V_B-range. From the logarithmic color scale of Fig. 3(a), it is evident that the photocurrent rises sharply, over the wavelength range of ~320 to 380 nm. For a bias voltage as small as $V_B = 1$ V, the measured photocurrent ($I_\lambda \sim 7.03$ nA) is nearly 3 orders-of-magnitude higher than the dark current ($I_D \sim 7.87$ pA), at the UV-A wavelength of $\lambda = 353$ nm. Conversely, the photocurrent ($I_\lambda \sim 42$ pA) is only six times the dark current, at the visible wavelength of $\lambda = 420$ nm (also measured at $V_B = 1$ V).

While four different carrier transport mechanisms were observed to contribute to the dark current measured at different bias voltages, TE appears to be the dominant mechanism

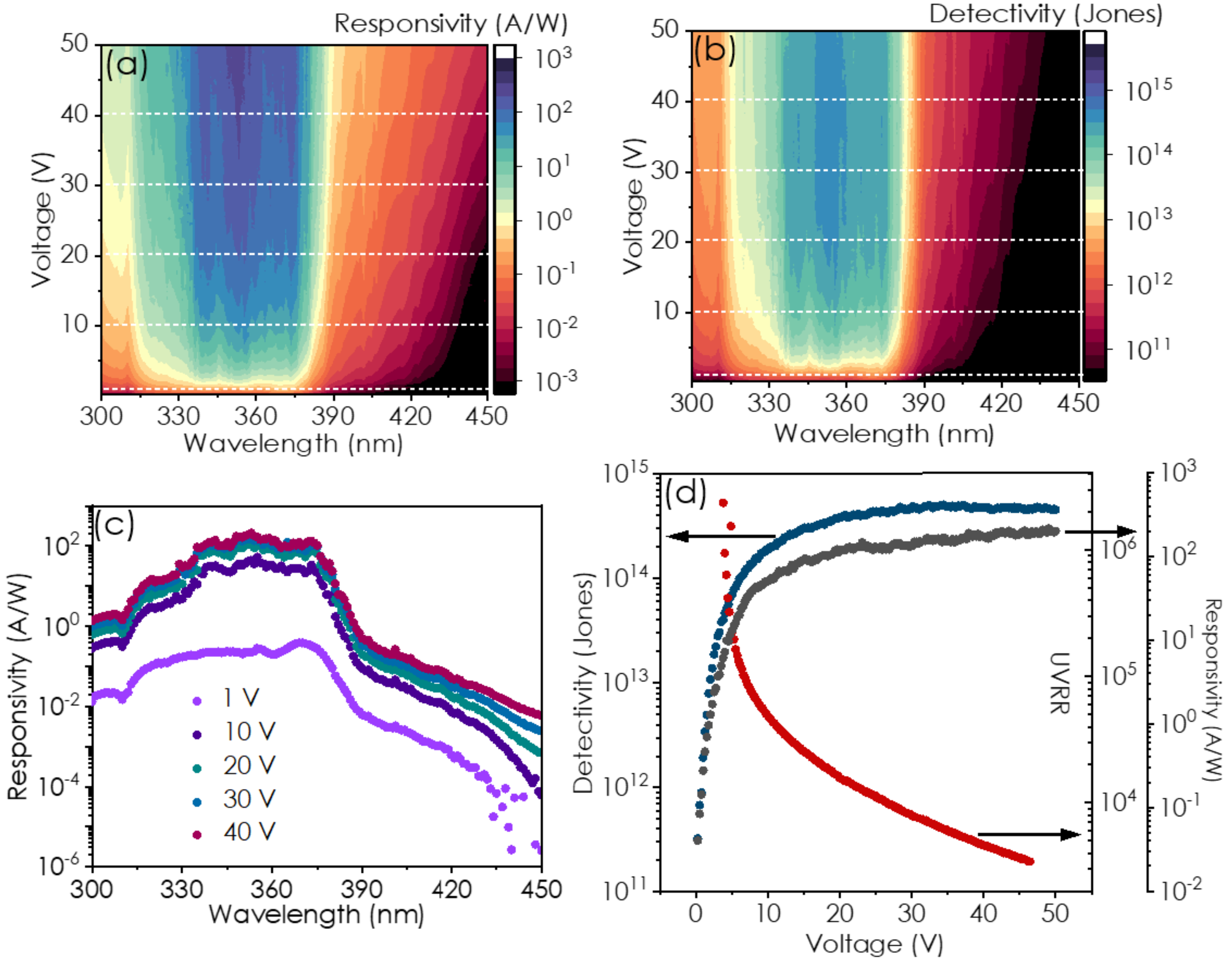

Fig. 4. Colormap of the calculated (a) responsivity and (b) specific detectivity, as a function of the applied bias (V_B) and the wavelength (λ) of the incident radiation. (c) Responsivity (R) versus λ, at different V_B [denoted by the white dashed lines in the colormap of (a)]. (d) V_B-dependence of specific detectivity (D) and responsivity (R), both for $\lambda = 355$ nm, and UVRR, defined as $r = R^{\lambda=353\text{nm}}/R^{\lambda=420\text{nm}}$.

governing the photocurrent, at different wavelengths. Fittings of the TE equation are also shown in Fig. 3(b), with $\eta = 1$.

An excellent fit is observed over the entire V_B-range, for illumination at all wavelengths, except $\lambda = 353$ nm. For this wavelength, the measured current is lower than that suggested by the TE model, for up to $V_B = 10$ V. This indicates the predominance of direct tunneling over TE. From the fits of the TE equation, we determined the zero-bias Schottky-barrier heights [$\Phi_B(\lambda)$] over the entire range of wavelengths. Subtracting these $\Phi_B(\lambda)$ values from the Φ_B obtained earlier from the $I_D - V_B$ characteristics, we calculated the photo-induced Schottky-barrier-height (SBH) lowering [$\Delta\Phi_B(\lambda)$], at different excitation wavelengths. The λ-dependence of $\Delta\Phi_B[\Delta\Phi_B(\lambda)]$ is shown in the inset of Fig. 3(b).

The responsivity ($R = (I_\lambda - I_D)/P_i$) and specific detectivity ($D = R(A)^{1/2}/(2qI_D)^{1/2}$) colormaps, as functions of both V_B and λ, are shown in Fig. 4(a) and (b), respectively. Here, P_i is the input optical power on the effective active-area (A) of the PD, while q is the electronic charge. Fig. 4(c) shows the plot of R versus λ, for five different bias-voltages indicated by the dotted lines in the colormap of Fig. 4(a). The λ-dependence of R appears to be the same, for all bias voltages, although the absolute value increases continuously with increasing V_B. As a representative value, we report $R(\lambda = 355 \text{ nm}) =$ 280 mA/W and 53 A/W, at $V_B = 1$ and 10 V, respectively. The V_B-dependence of the responsivity, at $\lambda = 355$ nm is explicitly shown in Fig. 4(d), where we observe values as high as 200 A/W. The values of $R(\lambda = 355 \text{ nm})$ exceed the theoretical value ($R = 290$ mA/W), for $V_B \geq 1$ V. This is true also for the wavelength range of $\lambda = 320$ – 380 nm [Fig. 4(b) and (c)], indicating that an internal gain mechanism is operational. We note that the λ-dependence of R is qualitatively similar to that of the SBH lowering ($\Delta\phi_B$), shown earlier in the inset of Fig. 3(b). Therefore, the internal gain in the MSM PDs may be attributed to hole-trapping, which leads to photo-induced SBH lowering [39].

The λ-dependence of the specific detectivity, D, follows the same trend as that of R (data not shown), since

TABLE I
COMPARISON OF THE DIFFERENT FOM OF GaN PDs REPORTED IN THE LITERATURE

[Ref.] Author (Year)	Dark Current (A)	Responsivity (A/W)	Rejection Ratio	Specific detectivity (Jones)	Rise Time (ms) (Fall Time (ms))	Metal stack (Thickness)
[27] Zhao (2000)	-	6.9@5V	10	-	4.8	Al
[26] Wang (2007)	-	4600@1V	1.8	-	-	Ni/Au (3/100 nm)
[30] Chuang (2007)	1.21×10^{-10}@$5V$	0.079@5V	43	3.9×10^{12}@$5V$	-	TiW (100 nm) Ni/Au (10/90 nm)
[15] Malinowski (2009)	20×10^{-15}@$-1V$	0.135@-1V	15000	4.5×10^{13}@$-1V$	-	Ti/Au/Mo/Au (10/40/25/50 nm) Au (15 nm)
[25] Chiang (2010)	1.21×10^{-10}@$5V$	0.138@5V	< 2	-	-	Au
[32] Chang (2013)	7.8×10^{-13}@$5V$	0.016@5V	2100	1.73×10^{10}@$5V$	-	TiW
[31] Saron (2013)	6.13×10^{-6}@$5V$	0.0285@5V	233	-	7.1 (10.4)	Ni (250 nm)
[24] Velazquez (2016)	-	0.212@2V	-	-	-	Al-Al, Al-Cu, Cu-Cu
[29] Lee (2017)	-	0.05@1V	-	-	-	ITO (100 nm)
[28] Ravikiran (2017)	4.3×10^{-10}@$5V$	0.183@15V	12000	5.5×10^{11}@$5V$	-	Ni/Au (150/350 nm)
[36] Jain (2018)	6.5×10^{-3}@$5V$	0.28@10V	-	-	14 (12)	Pt-Ag, Pt-Cr, Pt-Pt
[22] Krishna (2019)	100×10^{-3}@$5V$	2.1@1V	-	1.3×10^{9}@$1V$	81 (20) @1 V	Cr-Au
[23] Aggarwal (2019)	12×10^{-3}@$5V$	0.28@ 5 V 0.219 @ 5 V 0.2 @ 5 V	-	9.8×10^{9}@$5V$	80.5 (53) 52 (46.5) 47.4 (43.8)	Au Ti/Al Al
[20] Pokharia (2020)	4.7×10^{-9}@$15V$	33.3@15V	33.32	4.6×10^{12}@$15V$	3.5 (4)	Ni/Au (40/120 nm)
[21] Yadav (2022)	5.73×10^{-4}@1V	1.4×10^{3}@1 V	-	1.83×10^{12}	1140 (853) 539 (735) 47 (21)	Au Pd ITO
[18] Jiang (2022)	-	0.0714@1V	-	7.1×10^{8}	4000 (11900) As-prepared 220 (760) annealed	Au
This Work (2022)	8.5×10^{-12}@10V	53.01@10V	36336	4.93×10^{14}@13 V	0.084 (0.079)	Pt/Au

I_D is three-orders-of-magnitude smaller than the photocurrent, at $V_B \geq 1$ V. Together with $R(\lambda = 355$ nm$)$, $D(\lambda = 355$ nm$)$ is plotted as a function of V_B, in Fig. 4(d). While the value of D at 1 V is 2.4×10^{12} Jones, it saturates beyond ~13 V to ~4.93×10^{14} Jones.

Fig. 4(d) also shows the V_B-dependence of the UVRR, which we define as $r = R^{\lambda=353 \text{ nm}}/R^{\lambda=420 \text{ nm}}$. The UVRR is maximum at zero bias ($r = 2.41 \times 10^6$), while it reduces to 3.42×10^3, at $V_B = 50$ V. Comparing the value of the estimated UVRR at 15 V ($r = 2.3 \times 10^4$) with that of similar MSM devices with Ni/Au contacts ($r = 33$, [20]), we observe >100-fold enhancement.

The temporal response of the MSM PDs, recorded at different bias voltages, V_B (illumination-power, P_i), while keeping $P_i = 1$ mW ($V_B = 30$ V) constant, is shown in Fig. 5(a) [Fig 5(b)]. For these measurements, MSM PDs with a larger-active area have been probed, wherein the IDT consists of 10-μm-wide and 1-mm-long fingers, with consecutive fingers separated by 90 μm. This ensured that the entire photon flux was captured within the active area of the PDs. For a fixed P_i (V_B), the residual current in the OFF-state (I_{off}) is observed to increase consistently, for increasing V_B (P_i), in Fig. 5(a) [Fig. 5(b)]. This may be explained by an enhancement of the persistent component in the photocurrent, caused by charging and discharging of bulk traps. Several trapping centers, with characteristic times varying from microseconds to hours, have been considered in the literature [41], [42], [43], [44], [45], [46] to explain the microscopic origin of persistent-photoconductivity in GaN. However, such an investigation, which involves photocurrent

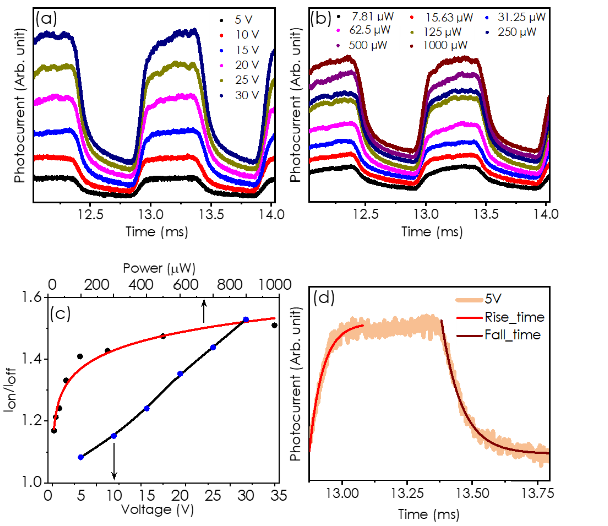

Fig. 5. Temporal photoresponse for illumination at $\lambda = 325$ nm at (a) different bias voltages between $V_B = 5$ and 30 V and (b) different illumination power levels between $P_i = 7.81$ μW and 1 mW. The illumination power in (a) is $P_i = 1$ mW, and the bias-voltage in (b) is $V_B = 30$ V. (c) Ratio of the ON and OFF currents as function of both bias-voltage and illumination power. (d) Exponential fitting to the rising and falling part of the temporal photoresponse used to estimate the rise time and fall-time, respectively.

measurements over a range of temperatures, is beyond the scope of this work. Nevertheless, the rise of I_{off} with increasing V_B may be attributed to increasing band-bending, and a concomitant enhancement of the PF effect.

Hence, the rise of I_{off} with increasing P_i may be ascribed to a higher concentration of trapped charges, which get trapped and re-emitted at the large (fixed) V_B.

Despite this increase in I_{off}, the ratio of the ON-current (I_{on}) to I_{off} increases, both with V_B and P_i [Fig. 5(c)]. This suggests that the photo-induced SBH lowering is predominant under illumination, leading to the observed gain in the MSM PDs. By fitting the rising and decaying parts of the temporal response with the equations $I(t) = I_{\text{off}} + A[1 - \exp(-\frac{t-t_0}{\tau_R})]$ and $I(t) = I_{\text{off}} + A[\exp(-\frac{t-t_0}{\tau_F})]$, respectively, we estimated the rise time (τ_R) and fall-time (τ_F) of the PDs [Fig. 5(d)]. A and t_0 in the above equations are the scaling constant and (ON and OFF) switching time, respectively. τ_R (τ_F) decreases (increases) monotonically from 84μs (79 μs) to 55μs (116 μs), when V_B is increased from 5 to 30 V. These values are nearly a decade lower than that observed in our earlier MSM PDs with Ni/Au contacts [20].

IV. Conclusion

In conclusion, we reported the fabrication and photoresponse characterization of GaN-based visible-blind MSM PDs, with back-to-back Pt/Au Schottky contacts, and demonstrated the maximum specific detectivity ($V_B \geq 13$ V) reported till date. Table I shows a comparison of the different figures of merit (FOM) of different GaN/Si PDs published in the literature. The high specific detectivity is obtained due to a very large responsivity of the PDs in the UV-A range, combined with a low dark current, even for bias voltages as high as 40 V. Responsivity values beyond the theoretical limit, measured for $V_B > 1$ V, indicates the presence of internal gain, which is mediated by photo-induced SBH lowering. While the response time measured in this work is among the lowest reported in the literature, the values are possibly limited by persistent photoconductivity, well-known for GaN. Further improvements in the time response, which may be achieved by improvement in epitaxial growth of GaN on Si, can pave the way for the development and commercialization of reliable and low-cost visible-blind PD arrays.

Acknowledgment

The authors would like to thank the IIT Bombay Nanofabrication Facility (IITBNF) for assistance with device fabrication.

References

[1] N. Shibata, "Fabrication of LEDs based on III–V nitrides and their applications," *Phys. Status Solidi*, vol. 192, no. 2, pp. 254–260, Aug. 2002.

[2] F. A. Ponce and D. P. Bour, "Nitride-based semiconductors for blue and green light-emitting devices," *Nature*, vol. 386, no. 6623, pp. 351–359, Mar. 1997.

[3] L. Liu and J. H. Edgar, "Substrate for gallium nitride epitaxy," *Mater. Sci. Eng., R, Rep.*, vol. 37, no. 3, pp. 61–127, 2002.

[4] J. Wu, "When group-III nitrides go infrared: New properties and perspectives," *J. Appl. Phys.*, vol. 106, no. 1, Jul. 2009, Art. no. 011101.

[5] C. Zhou et al., "Review—The current and emerging applications of the III-nitrides," *ECS J. Solid State Sci. Technol.*, vol. 6, no. 12, pp. Q149–Q156, 2017.

[6] D. Walker et al., "Visible blind GaN *p-i-n* photodiodes," *Appl. Phys. Lett.*, vol. 72, no. 25, pp. 3303–3305, Jun. 1998.

[7] G. Hellings, J. John, A. Lorenz, P. Malinowski, and R. Mertens, "AlGaN Schottky diodes for detector applications in the UV wavelength range," *IEEE Trans. Electron Devices*, vol. 56, no. 11, pp. 2833–2839, Nov. 2009.

[8] E. Muñoz, "(Al,In,Ga)N-based photodetectors. Some materials issues," *Phys. Status Solidi*, vol. 244, no. 8, pp. 2859–2877, Aug. 2007.

[9] L. S. Chuah, Z. Hassan, H. A. Hassan, and M. H. Mourad, "p-GaN/n-Si heterojunction photodiodes," *Surf. Rev. Lett.*, vol. 15, no. 5, pp. 699–703, 2008.

[10] H. Ohta, N. Asai, F. Horikiri, Y. Narita, T. Yoshida, and T. Mishima, "Two-step mesa structure GaN p-n diodes with low ON-resistance, high breakdown voltage, and excellent avalanche capabilities," *IEEE Electron Device Lett.*, vol. 41, no. 1, pp. 123–126, Jan. 2020.

[11] P. Kung, X. Zhang, D. Walker, A. W. Saxler, and M. Razeghi, "GaN p-i-n photodiodes with high visible-to-ultraviolet rejection ratio," in *Proc. SPIE*, 1998, pp. 214–220.

[12] G. Parish et al., "High-performance (Al,Ga)N-based solar-blind ultraviolet p–i–n detectors on laterally epitaxially overgrown GaN," *Appl. Phys. Lett.*, vol. 75, no. 2, pp. 247–249, Jul. 1999.

[13] Y. Huang et al., "Back-illuminated separate absorption and multiplication AlGaN solar-blind avalanche photodiodes," *Appl. Phys. Lett.*, vol. 101, no. 25, Dec. 2012, Art. no. 253516.

[14] O. Katz, V. Garber, B. Meyler, G. Bahir, and J. Salzman, "Gain mechanism in GaN Schottky ultraviolet detectors," *Appl. Phys. Lett.*, vol. 79, no. 10, pp. 1417–1419, Sep. 2001.

[15] P. E. Malinowski et al., "Backside-illuminated GaN-on-Si Schottky photodiodes for UV radiation detection," *IEEE Electron Device Lett.*, vol. 30, no. 12, pp. 1308–1310, Dec. 2009.

[16] C. Wang et al., "GaN MSM UV photodetector with sputtered AlN nucleation layer," *IEEE Sensors J.*, vol. 15, no. 9, pp. 4743–4748, Sep. 2015.

[17] S. Chang, M. Chang, and Y. Yang, "Enhanced responsivity of GaN metal–semiconductor–metal(MSM) photodetectors on GaN substrate," *IEEE Photon. J.*, vol. 9, no. 2, Apr. 2017, Art. no. 6801707.

[18] H.-H. Jiang et al., "GaN MSM structure UV photodetector detector based on nonplanar Si substrate and its performance optimization," *Semiconductor Sci. Technol.*, vol. 37, no. 10, Oct. 2022, Art. no. 105020.

[19] E. Monroy, T. Palacios, O. Hainaut, F. Omnès, F. Calle, and J.-F. Hochedez, "Assessment of GaN metal–semiconductor–metal photodiodes for high-energy ultraviolet photodetection," *Appl. Phys. Lett.*, vol. 80, no. 17, pp. 3198–3200, Apr. 2002.

[20] R. S. Pokharia et al., "A highly sensitive and robust GaN ultraviolet photodetector fabricated on 150-mm Si (111) wafer," *IEEE Trans. Electron Devices*, vol. 68, no. 6, pp. 2796–2803, Jun. 2021.

[21] G. Yadav, V. Gupta, and M. Tomar, "Double Schottky metal–semiconductor–metal based GaN photodetectors with improved response using laser MBE technique," *J. Mater. Res.*, vol. 37, no. 2, pp. 457–469, Jan. 2022.

[22] S. Krishna et al., "Correlation of donor-acceptor pair emission on the performance of GaN-based UV photodetector," *Mater. Sci. Semiconductor Process.*, vol. 98, pp. 59–64, Aug. 2019.

[23] N. Aggarwal et al., "Impact on photon-assisted charge carrier transport by engineering electrodes of GaN based UV photodetectors," *J. Alloys Compounds*, vol. 785, pp. 883–890, May 2019.

[24] R. Velazquez, A. Aldalbahi, M. Rivera, and P. Feng, "Fabrications and application of single crystalline GaN for high-performance deep UV photodetectors," *AIP Adv.*, vol. 6, no. 8, Aug. 2016, Art. no. 085117.

[25] Y.-T. Chiang et al., "GaN on silicon substrate with various SiC buffer layer for UV detecting applications," *IEEE Sensors J.*, vol. 10, no. 8, pp. 1291–1296, Aug. 2010.

[26] X. Wang et al., "High responsivity ultraviolet photodetector based on crack-free GaN on Si(111)," *Physica. Status Solidi*, vol. 4, no. 5, pp. 1613–1616, 2007.

[27] Z. M. Zhao et al., "Metal–semiconductor–metal GaN ultraviolet photodetectors on Si(111)," *Appl. Phys. Lett.*, vol. 77, no. 3, pp. 444–446, 2000.

[28] L. Ravikiran et al., "GaN Schottky metal–semiconductor–metal UV Photodetectors on Si(111) grown by ammonia-MBE," *IEEE Sensors J.*, vol. 17, no. 1, pp. 71–77, Oct. 2017.

[29] C.-J. Lee, C.-H. Won, J.-H. Lee, S.-H. Hahm, and H. Park, "Selectively enhanced UV-A photoresponsivity of a GaN MSM UV photodetector with a step-graded Al_xGa1_xN buffer layer," *Sensors*, vol. 17, no. 7, p. 1684, Jul. 2017.

[30] R. W. Chuang et al., "Gallium nitride metal-semiconductor-metal photodetectors prepared on silicon substrate," *J. Appl. Phys.*, vol. 102, no. 7, 2007, Art. no. 073110.

[31] K. M. A. Saron, M. R. Hashim, and M. A. Farrukh, "Growth of GaN films on silicon (111) by thermal vapor deposition method: Optical functions and MSM UV photodetector applications," *Superlattices Microstructures*, vol. 64, pp. 88–97, Dec. 2013.

[32] S. J. Chang, R. W. Chuang, and S. P. Chang, "Fabrication of crack-free metal–semiconductor–metal ultraviolet photodetectors on Si(111) substrates based on novel AlN/AlGaN buffer multilayer scheme," *ECS Trans.*, vol. 11, no. 5, pp. 117–128, 2013.

[33] A. Kadir et al., "Influence of substrate nitridation on the threading dislocation density of GaN grown on 200 mm Si (111) substrate," *Thin Solid Films*, vol. 663, pp. 73–78, Oct. 2018.

[34] J. Meyer, R. Liu, R. D. Schaller, H.-P. Lee, and C. Bayram, "Systematic study of Shockley-read-Hall and radiative recombination in GaN on Al_2O_3, freestanding GaN, and GaN on Si," *J. Phys., Photon.*, vol. 2, no. 3, Jul. 2020, Art. no. 035003.

[35] H. P. D. Schenk, E. Frayssinet, A. Bavard, D. Rondi, Y. Cordier, and M. Kennard, "Growth of thick, continuous GaN layers on 4-in. Si substrates by metalorganic chemical vapor deposition," *J. Cryst. Growth*, vol. 314, no. 1, pp. 85–91, Jan. 2011.

[36] S. K. Jain et al., "GaN-UV photodetector integrated with asymmetric metal semiconductor metal structure for enhanced responsivity," *J. Mater. Sci., Mater. Electron.*, vol. 29, no. 11, pp. 8958–8963, Jun. 2018.

[37] J. G. Wright, C. S. Chang, D. A. Müller, H. G. Xing, and D. Jena, "Structural and electronic properties of NbN/GaN junctions grown by molecular beam epitaxy," *APL Mater.*, vol. 10, no. 5, May 2022, Art. no. 051103.

[38] H. Sheoran, B. R. Tak, N. Manikanthababu, and R. Singh, "Temperature-dependent electrical characteristics of Ni/Au vertical Schottky barrier diodes on γ-Ga_2O_3 epilayers," *ECS J. Solid State Sci. Technol.*, vol. 9, no. 5, Jan. 2020, Art. no. 055004.

[39] U. U. Muazzam, P. C. Chavan, R. Muralidharan, S. Raghavan, and D. N. Nath, "Optical properties of mist CVD grown k-Ga_2O_3," *Semicond. Sci. Technol.*, vol. 37, Apr. 2022, Art. no. 055011.

[40] S. Rathkanthiwar et al., "Gain mechanism and carrier transport in high responsivity AlGaN-based solar blind metal semiconductor metal photodetectors," *J. Appl. Phys.*, vol. 121, no. 16, Apr. 2017, Art. no. 164502.

[41] M. Hou, H. So, A. J. Suria, A. S. Yalamarthy, and D. G. Senesky, "Suppression of persistent photoconductivity in AlGaN/GaN ultraviolet photodetectors using in situ heating," *IEEE Electron Device Lett.*, vol. 38, no. 1, pp. 56–59, Jan. 2017.

[42] J. Z. Li, J. Y. Lin, H. X. Jiang, M. A. Khan, and Q. Chen, "Persistent photoconductivity in a two-dimensional electron gas system formed by an AlGaN/GaN heterostructure," *J. Appl. Phys.*, vol. 82, no. 3, pp. 1227–1230, Aug. 1997.

[43] M. T. Hirsch, J. A. Wolk, W. Walukiewicz, and E. E. Haller, "Persistent photoconductivity in n-type GaN," *Appl. Phys. Lett.*, vol. 71, no. 8, pp. 1098–1100, Aug. 1997.

[44] H. M. Chen, Y. F. Chen, M. C. Lee, and M. S. Feng, "Persistent photoconductivity in N-type GaN," *J. Appl. Phys.*, vol. 82, no. 2, pp. 899–901, Jul. 1997.

[45] G. Beadie, W. S. Rabinovich, A. E. Wickenden, D. D. Koleske, S. C. Binari, and J. A. Freitas, "Persistent photoconductivity in N-type GaN," *Appl. Phys. Lett.*, vol. 71, no. 8, pp. 1092–1094, Aug. 1997.

[46] C. H. Qiu and J. I. Pankove, "Deep levels and persistent photoconductivity in GaN thin films," *Appl. Phys. Lett.*, vol. 70, no. 15, pp. 1983–1985, Apr. 1997.